

# Analysis of dynamic bipedal robot walking with stick-slip transitions

Benny Gamus and Yizhar Or

Faculty of Mechanical Engineering, Technion, Haifa 32000, Israel.

**Abstract—** This paper studies the hybrid dynamics of simple biped robot models under possible stick-slip transitions. Unlike almost all existing works in the literature that assume perfect sticking of the stance foot, we explore the case of insufficient friction which induces foot slippage. Numerical simulations of passive dynamic walking reveal the onset of stable periodic solutions that involve stick-slip transitions. In the case of a biped with joint torques actuation, we demonstrate how one can induce and stabilize stick-slip gaits which significantly reduce the energetic cost of walking and enforce slippage even for high friction.

**Keywords-** *Passive Walking; Contact Modelling*

## I. INTRODUCTION

In mobile robots, legged locomotion is commonly used in order to negotiate unstructured terrains or indoor environments where traditional wheeled and tracked vehicles have limited maneuverability or accessibility. Analysis and control of legged robots are currently subject to extensive research efforts, motivated primarily by the need to develop autonomous mobile robots for various applications such as military and security [1], rehabilitation assistance [2], education and entertainment [3,4] and even planetary exploration [5,6]. Unlike quasistatic locomotion, in which the robot moves slowly through a sequence of equilibrium postures, in *dynamic* legged locomotion (DLL) the robot constantly undergoes unsteady motion of falling, followed by placement of a free foot on the ground and transfer of the support in a cyclic pattern (i.e. gait). Many works on legged robots are inspired by biological locomotion of insects and large animals [7,8], e.g. the well-known RHEX robot [9]. The dynamics of legged locomotion is typically governed by highly nonlinear ODE's that are interleaved with discrete events of "jumps" induced by foot impacts and contact transitions, giving rise to a hybrid dynamical system with nonsmooth behavior [10,11]. One of the most classical and simple models of DLL is McGeer's bipedal walker [12] which is a two-link robot that walks passively down a shallow slope. The dynamics of the two-link model, named *compass biped*, is further analyzed by Goswami in [13]. In his work [12], McGeer also introduces and analyzes an even simpler and low-dimensional model – *the rimless spoked wheel*, which is further analyzed by Coleman and Ruina [14]. A central theme in DLL is the orbital stability of the hybrid periodic solutions, which can be assessed via linearization of the Poincaré map [15]. Stability can be achieved either passively as in [12-14], or by using active feedback control of the motor torques at the robot's joints according to sensory information [16,17]. Feedback

control of DLL has been a highly active field of research in the last decade. Focusing on bipedal robots, sophisticated nonlinear techniques have been employed, with emphasis on advanced geometric notions such as controlled symmetries [18], Routhian reduction [19], zero dynamics [20], transverse linearization [21] and virtual nonholonomic constraints [22]. A key limitation of all the theoretical models mentioned above is that they assume that the foot-ground contact is a stationary pivot point, and that no foot slippage occurs throughout the motion and during impacts. This assumption is not always physically realistic, since it requires that friction at the contact is sufficiently large in order to enforce sticking. Moreover, perturbations caused by external forces, vibrations, or local surface irregularity can kinematically impose initial foot slippage even for large friction. Additionally, experimental measurements indicate that foot slippage is ubiquitous also in biological legged locomotion [23,24]. While few works incorporated friction considerations in designing gaits that avoid slippage [25,26], and some works studied detection and estimation of slippage from sensory data [27], the dynamics of legged locomotion with possible stick-slip transitions has rarely been considered. (An exception is the two-link hopper analyzed in [28]).

The goal of this paper is to study simple models of bipedal dynamic walking that involve stick-slip transitions at the feet assuming Coulomb's dry friction model, and numerically investigate the effect of foot slippage. The paper studies the models of rimless spoked wheel and the compass biped under passive dynamics on a slope, and also the controlled torque-actuated compass biped on a horizontal plane. When the friction is not sufficient to maintain contact sticking, foot slippage starts to evolve. Numerical simulations reveal the existence of periodic solutions that involve foot slippage and stick-slip transitions. In the case of a torque-actuated compass biped, some of these gaits have improved energetic efficiency compared to sticking gaits, and can be stabilized via feedback control. The structure of the paper is as follows. The next section gives a general formulation of the equations of motion. Section III studies the rimless spoked wheel, Section IV studies the passive compass biped on a slope, and Section V studies the torque-actuated compass biped on a horizontal plane.

## II. GENERAL FORMULATION

We now formulate the equations of motion of a general bipedal robot consisting of rigid links, which walks on a plane in two dimensions. It is assumed that one foot (the "stance foot") of the robot maintains point contact with the ground,

while the other foot (the ‘‘swing foot’’) is free. When the swing foot hits the ground an impact occurs, followed by an instantaneous velocity change, and the feet switch roles. The motion then continues in a cyclic pattern.

#### A. Continuous-time equations

Let  $\mathbf{q} \in \mathbb{R}^N$  be the coordinates describing the robot’s configuration. The velocity of the stance foot’s endpoint can be decomposed into components normal and tangent to the ground as  $v_n = \mathbf{w}_n(\mathbf{q}) \cdot \dot{\mathbf{q}}$  and  $v_t = \mathbf{w}_t(\mathbf{q}) \cdot \dot{\mathbf{q}}$ . When the contact point is stationary, the velocities satisfy the constraint

$$\mathbf{W}(\mathbf{q})\dot{\mathbf{q}} = \begin{bmatrix} \mathbf{w}_t^T(\mathbf{q}) \\ \mathbf{w}_n^T(\mathbf{q}) \end{bmatrix} \dot{\mathbf{q}} = 0. \quad (1)$$

The robot’s dynamic equations of motion are given by Euler-Lagrange equations as (cf. [29]):

$$\mathbf{M}(\mathbf{q}) \cdot \ddot{\mathbf{q}} + \mathbf{B}(\mathbf{q}, \dot{\mathbf{q}}) + \mathbf{G}(\mathbf{q}) = \mathbf{E}\mathbf{u} + \mathbf{W}^T \mathbf{f}, \quad (2)$$

where  $\mathbf{u} \in \mathbb{R}^m$  are controlled input torques (if they exist) and  $\mathbf{f} = [f_t \quad f_n]^T$  are the tangential and normal components of the contact force which enforces the constraint (1). Note that  $\mathbf{W}(\mathbf{q})$  in (1) and (2) can be interpreted as the robot’s Jacobian with respect to the contact point, and that  $\mathbf{f}$  can be regarded as the vector of Lagrange multipliers, cf. [29]. The state vector of the system  $\mathbf{x}$  augments the positions and velocities  $\mathbf{x} = (\mathbf{q}, \dot{\mathbf{q}})^T$ . In order to compute the contact force  $\mathbf{f}$ , one has to differentiate the constraint (1) with respect to time and substitute the expression for the accelerations  $\ddot{\mathbf{q}}$  from (2) in order to obtain (cf. [29]):

$$\mathbf{f}(\mathbf{q}, \dot{\mathbf{q}}) = \left( \mathbf{W}\mathbf{M}^{-1}\mathbf{W}^T \right)^{-1} \left( \mathbf{W}\mathbf{M}^{-1}(\mathbf{B} + \mathbf{G} - \mathbf{E}\mathbf{u}) - \dot{\mathbf{W}}\dot{\mathbf{q}} \right), \quad (3)$$

where the dependence on  $\mathbf{q}, \dot{\mathbf{q}}$  on the right hand side of (3) is suppressed for brevity. Importantly, the constraint (1) can be enforced only if the contact force  $\mathbf{f}$  in (3) satisfies the friction constraint given by

$$|f_t| \leq \mu f_n \quad (4)$$

where  $\mu$  is Coulomb’s coefficient of friction. When inequality (4) is not satisfied, tangential slippage of the contact point starts to evolve, i.e.  $v_t \neq 0$ . In that case, according to Coulomb’s friction model, the tangential contact force  $f_t$  opposes the direction of slippage, and depends on the normal force  $f_n$  as

$$f_t = -\mu \operatorname{sgn}(v_t) f_n. \quad (5)$$

(For simplicity, we do not distinguish between static and kinetic friction throughout this work). The contact force  $\mathbf{f}$  under slippage cannot be computed as in (3). Instead, differentiation of  $\mathbf{w}_n(\mathbf{q}) \cdot \dot{\mathbf{q}} = 0$  and using (2) and (5) gives:

$$f_n(\mathbf{q}, \dot{\mathbf{q}}) = \left( \mathbf{w}_n^T \mathbf{M}^{-1} \Gamma \right)^{-1} \left( \mathbf{w}_n^T \mathbf{M}^{-1} (\mathbf{B} + \mathbf{G} - \mathbf{E}\mathbf{u}) - \dot{\mathbf{w}}_n^T \dot{\mathbf{q}} \right), \quad (6)$$

where  $\Gamma(\mathbf{q}) = \mathbf{w}_n(\mathbf{q}) - \mu \operatorname{sgn}(v_t) \mathbf{w}_t(\mathbf{q})$ , while  $f_t$  is determined according to (5). Contact slippage occurs until  $v_t$  vanishes.

Then, a transition to sticking contact occurs, if the contact force  $\mathbf{f}$  in (3) satisfies (4). Otherwise, slip reversal occurs and  $v_t$  changes its sign.

#### B. Impact law

The tangential and normal velocities of the swing foot are given by

$$\tilde{\mathbf{v}}_{swing} = \begin{bmatrix} \tilde{v}_t \\ \tilde{v}_n \end{bmatrix} = \tilde{\mathbf{W}}(\mathbf{q})\dot{\mathbf{q}} = \begin{bmatrix} \tilde{\mathbf{w}}_t^T(\mathbf{q}) \\ \tilde{\mathbf{w}}_n^T(\mathbf{q}) \end{bmatrix} \dot{\mathbf{q}}. \quad (7)$$

When the swing foot hits the ground, an impact occurs. It is assumed that impulsive contact force  $\tilde{\mathbf{F}}$  at the colliding foot causes instantaneous change in the velocities at the time of impact  $t=t_{\#}$ , while the configuration  $\mathbf{q}$  remains unchanged  $\mathbf{q}=\mathbf{q}_{\#}$ . The velocity jump due to the impact is then given by

$$\dot{\mathbf{q}}(t_{\#}^+) - \dot{\mathbf{q}}(t_{\#}^-) = \mathbf{M}_{\#}^{-1} \tilde{\mathbf{W}}_{\#}^T \tilde{\mathbf{F}} \quad (8)$$

where the superscript ‘+’ denotes the time right after the impact while the superscript ‘-’ denotes the time right before it. The subscripts ‘#’ in (8) indicate that  $\mathbf{M}(\mathbf{q})$  and  $\tilde{\mathbf{W}}(\mathbf{q})$  are evaluated at  $\mathbf{q}=\mathbf{q}_{\#}$ . For more details on derivation of the impact equations see for example [11,30] and [31].

It is commonly assumed that the impact is perfectly plastic. That is, it results in sticking contact at the colliding foot, i.e.  $\tilde{\mathbf{v}}_{swing}(t_{\#}^+) = 0$ . Using (7) and (8), the contact impulse can then be obtained as:

$$\tilde{\mathbf{F}} = - \left( \tilde{\mathbf{W}}\mathbf{M}_{\#}^{-1}\tilde{\mathbf{W}}_{\#}^T \right)^{-1} \tilde{\mathbf{W}}\dot{\mathbf{q}}_{\#}^-. \quad (9)$$

Substituting (9) into (8) then gives a linear relation between the post-impact and pre-impact velocities  $\dot{\mathbf{q}}_{\#}^+, \dot{\mathbf{q}}_{\#}^-$ . Typically, after the impact the coordinates are also relabeled in order to reflect the exchange of roles of the two legs. Thus, the change of the state vector  $\mathbf{x}$  is expressed by the linear transformation  $\mathbf{x}_{\#}^+ = \chi(\mathbf{q}_{\#}) \mathbf{x}_{\#}^-$ .

The assumption of a perfectly plastic impact that induces contact sticking holds only if the components of the contact impulse  $\tilde{\mathbf{F}}$  given in (9) satisfy the friction constraint

$$|\tilde{F}_t| \leq \mu \tilde{F}_n. \quad (10)$$

If this constraint is not satisfied, the impact must induce contact slippage, i.e.  $\tilde{v}_t(t_{\#}^+) \neq 0$ . Assuming no rebound, i.e.  $\tilde{v}_n(t_{\#}^+) = 0$ , the normal contact impulse can then be obtained as

$$\tilde{F}_n = - \left( \tilde{\mathbf{w}}_n^T(\mathbf{q}_{\#}) \mathbf{M}_{\#}^{-1} \tilde{\Gamma}^T \right)^{-1} \tilde{\mathbf{w}}_n^T(\mathbf{q}_{\#}) \dot{\mathbf{q}}_{\#}^-, \quad (11)$$

where  $\tilde{\Gamma} = \tilde{\mathbf{w}}_n(\mathbf{q}_{\#}) - \mu \operatorname{sgn}(v_t(t_{\#}^+)) \tilde{\mathbf{w}}_t(\mathbf{q}_{\#})$ . The tangential impulse is then obtained as  $\tilde{F}_t = -\mu \operatorname{sgn}(v_t(t_{\#}^+)) \tilde{F}_n$ .

#### C. Hybrid periodic solutions and their stability

In order to study periodic solutions of the biped’s hybrid dynamics (i.e. gaits) and assess their stability, we briefly introduce the notions of post-impact Poincaré section and Poincaré map (also called ‘stride map’ in [8]). The Poincaré section  $\Sigma$  is a codimension-1 subspace of the state space which

corresponds to post-impact states. The Poincaré map, defined as  $\Pi: \Sigma \rightarrow \Sigma$ , maps an initial state  $\mathbf{x}_0$  at a post-impact time to the post-impact state  $\mathbf{x}_\#^+$  right after the next impact. A periodic solution of the hybrid dynamics corresponds to a post-impact state  $\mathbf{x}^*$  which is a fixed point of the Poincaré map, i.e.  $\Pi(\mathbf{x}^*) = \mathbf{x}^*$ . Typically, the Poincaré map and its fixed point cannot be determined analytically, except for extremely simplified models without slippage such as [14] and [32]. Instead, one usually has to compute them via numerical integration of (2). The local stability of a gait is determined by the linearization matrix of the Poincaré map about its fixed point, denoted  $D\Pi(\mathbf{x}^*)$ , as follows. The gait is asymptotically stable under local state perturbations iff all eigenvalues of the linearization matrix  $D\Pi(\mathbf{x}^*)$  lie inside the unit disc in the complex plane. Loosely speaking, an eigenvalue  $\lambda$  corresponds to deviations from  $\mathbf{x}^*$  that behave as the series  $\lambda^k$  where  $k$  is the index of the impact events. (To be more precise, note that  $\Pi$  does not account for the coordinate of forward motion, and is thus restricted to a lower-dimensional subspace of  $\Sigma$ , see [17] for more details and formal definitions).

### III. THE RIMLESS WHEEL

In this section, the dynamics of the rimless wheel model [12,14] is considered. The rimless wheel is a star-like rigid body which consists of  $n$  evenly spaced spokes of length  $l$ , see Fig. 1. The mass of the body is  $m$  and its moment of inertia with respect to the center-of-mass is  $I_c$ . The wheel rolls on an inclined plane with slope angle  $\alpha$ . The lower spoke is in contact with the ground and represents the stance foot, until the next spoke, representing the swing foot, hits the ground. The unconstrained coordinates are  $\mathbf{q} = (x, y, \theta)$  where  $(x, y)$  denote the position of the contact point and  $\theta$  is the orientation of the lower spoke relative to the contact normal, which changes within the range  $[-\pi/n, \pi/n]$ . The wheel's equations of motion are given in (2) and (8), where

$$\mathbf{M} = \begin{bmatrix} m & 0 & ml \cos \theta \\ 0 & m & -ml \sin \theta \\ ml \cos \theta & -ml \sin \theta & ml^2(1 + \kappa) \end{bmatrix} \quad \mathbf{B} = \begin{bmatrix} -ml \sin \theta \cdot \dot{\theta}^2 \\ -ml \cos \theta \cdot \dot{\theta}^2 \\ 0 \end{bmatrix} \quad \mathbf{E} \mathbf{u} = 0$$

$$\mathbf{G} = mg \begin{bmatrix} -\sin \alpha \\ \cos \alpha \\ -l \sin(\alpha + \theta) \end{bmatrix} \quad \mathbf{W} = \begin{bmatrix} 1 & 0 & 0 \\ 0 & 1 & 0 \end{bmatrix} \quad \tilde{\mathbf{W}}_\# = \begin{bmatrix} 1 & 0 & 0 \\ 0 & 1 & -2l \sin \frac{\pi}{n} \end{bmatrix}$$

(12)

and  $\kappa = I_c / ml^2$  is the inertia ratio satisfying  $0 \leq \kappa \leq 1$ .

#### A. No-slip dynamics – review

We now briefly review the analysis of the wheel's dynamics in [14], which assumed that the contact point is always sticking. This assumption implies  $x=y=0$ , hence the single coordinate  $\theta$  is governed by an inverted pendulum equation:

$$\ddot{\theta} - \sin(\alpha + \theta) = 0, \quad (13)$$

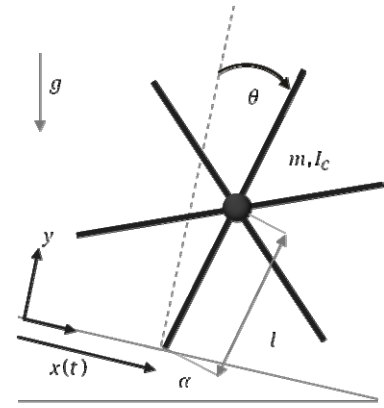


Fig. 1: The rimless wheel model.

where time is normalized by the characteristic time

$t_c = \sqrt{mgl / (ml^2 + I_c)}$ . Eq. (13) is integrable due to conservation of total mechanical energy, which gives the relation

$$\dot{\theta}^2 = \dot{\theta}_0^2 + 2 \cos\left(\alpha - \frac{\pi}{n}\right) - 2 \cos(\alpha + \theta). \quad (14)$$

where  $\dot{\theta}_0 = \dot{\theta}(0)$  is the initial angular velocity. Denoting the state vector as  $\mathbf{x} = (\theta, \dot{\theta})^T$ , the impact law under sticking contact (9) followed by spokes relabeling is given by

$$\mathbf{x}_\#^+ = \begin{bmatrix} -1 & 0 \\ 0 & \beta \end{bmatrix} \mathbf{x}_\#^-, \quad \text{where } \beta = \frac{\cos(2\pi/n) + \kappa}{1 + \kappa}. \quad (15)$$

Impact occurs when the next spoke hits the ground at angle  $\theta_\# = \pi/n$  (i.e. this defines the Poincaré section  $\Sigma$ ). Substituting the relation (14) and the impact law (15), the Poincaré map  $\Pi$  which is a scalar map from initial angular velocity  $\dot{\theta}_0$  to post-impact velocity  $\dot{\theta}_\#^+$  is derived analytically in [14], and its fixed point, which corresponds to a periodic solution, is obtained as:

$$\dot{\theta}^* = 2\beta \sqrt{\sin(\alpha) \sin(\pi/n) / (1 - \beta^2)}. \quad (16)$$

The linearization  $D\Pi(\dot{\theta}^*)$  is also derived in [14] as  $D\Pi(\dot{\theta}^*) = \beta^2 < 1$ , which is also the eigenvalue  $\lambda$ . This implies that the periodic solution is always locally asymptotically stable. Fig. 2 plots the periodic trajectory in  $(\theta, \dot{\theta})$  plane for  $n=10$ ,  $\kappa=1/3$  and  $\alpha=13^\circ$  (solid curve). The vertical line indicates the velocity jump due to impact, and the horizontal line represents the resetting of  $\theta$  from  $\pi/n$  back to  $-\pi/n$  due to interchange of the spokes.

One limitation which was not considered in [12,14] is the fact that the rimless wheel can maintain contact with the ground only if the normal contact force satisfies  $f_n \geq 0$  throughout the entire motion, otherwise the contact will detach. Using (3), the normal contact force is obtained as

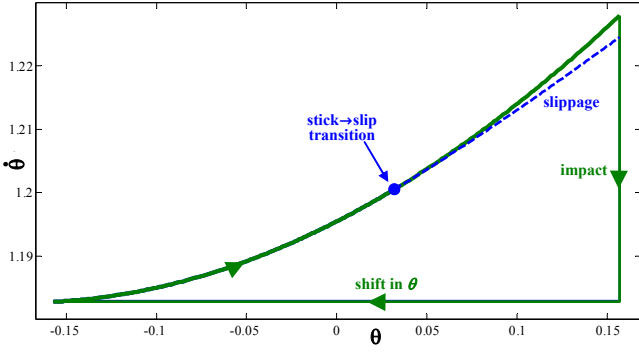


**Fig. 2:** Trajectories in  $(\theta, \dot{\theta})$  plane for periodic solutions with contact sticking (solid) and stick-slip (dashed)

$$f_n(\theta, \dot{\theta}) = \frac{gm}{1+\kappa} \left[ (\cos(\alpha + \theta) - \dot{\theta}^2) \cos \theta + \kappa \cos \alpha \right] \quad (17)$$

Substituting the relation (14) and the initial condition  $\dot{\theta}_0 = \dot{\theta}^*$  in (16) which corresponds to the periodic solution, one obtains an inequality constraint in  $\theta$  and the wheel's parameters  $n, \kappa, \alpha$  for which the periodic motion is possible without contact detachment. (Details are omitted due to space limitation.)

### B. Stick-slip dynamics

We now analyze the dynamics of the rimless wheel under possible transitions between sticking contact (as in [12,14]) to slippage. According to inequality (4), the assumption of contact sticking holds as long as the ratio of tangential to normal components of the contact force, defined by  $\sigma = f_t/f_n$ , satisfies  $|\sigma| < \mu$ , where  $\mu$  is the coefficient of friction. Using (3), the expression for  $\sigma$  is given by

$$\sigma(\theta, \dot{\theta}) = \frac{f_t}{f_n} = \frac{(\cos(\alpha + \theta) - \dot{\theta}^2) \sin \theta - \kappa \sin \alpha}{(\cos(\alpha + \theta) - \dot{\theta}^2) \cos \theta + \kappa \cos \alpha} \quad (18)$$

Substituting the relation (14) and the initial condition  $\dot{\theta}_0 = \dot{\theta}^*$ , one obtains the ratio  $\sigma(\theta)$  along the periodic solution. Sticking contact can be enforced along the entire continuous-time dynamics of the periodic solution as long as the coefficient of friction satisfies  $\mu \geq \mu_c$ , where  $\mu_c = \max\{|\sigma(\theta)|\}$ . Fig. 3 plots  $\sigma(\theta)$  for parameter values  $n=10$ ,  $\kappa=1/3$  and  $\alpha=13^\circ$ , for which one obtains  $\mu_c=0.91$ . In the following numerical simulations, the same values for  $n, \kappa$  and  $\alpha$  are used while the friction coefficient  $\mu$  is varied.

In order to ensure contact sticking also at the impact, the contact impulse must satisfy the frictional inequality (10). Assuming that at the pre-impact time the contact is sticking (i.e.  $\dot{x}_\#^- = 0$ ), this yields the inequality

$$|\tilde{\sigma}| = \left| \frac{\tilde{F}_t}{\tilde{F}_n} \right| = \left| \frac{\sin(2\pi/n)}{2[\kappa + \cos^2(\pi/n)]} \right| < \mu. \quad (19)$$

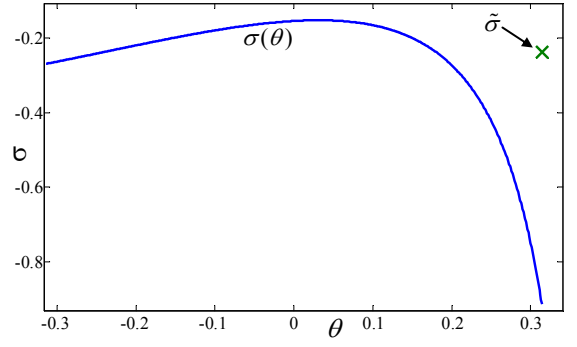


**Fig. 3:** The force ratio  $\sigma$  vs.  $\theta$  along the periodic solution

It can be shown (details omitted) that as long as  $\kappa > 0$ , one obtains  $|\tilde{\sigma}| < |\sigma|$ . That is, if the contact does not slip during the continuous-time motion along the periodic solution then it will also not slip due to the impact. This is demonstrated in Fig. 3 where the value of  $\tilde{\sigma}$  is marked as 'x' at the right end of the plot, and satisfies  $|\tilde{\sigma}| = 0.24 < \mu_c$ .

When the coefficient of friction is lower than the critical value  $\mu < \mu_c$ , the periodic solution without contact slippage cannot be maintained and contact slippage  $\dot{x}(t) \neq 0$  starts to evolve. Using (2), (5) and (6), The rimless wheel's equations of motion under contact slippage are given by

$$\begin{aligned} \ddot{\theta} &= \frac{\text{sgn}(\dot{x}) \mu \cos \theta \cdot f_n + m \sin \theta (g \cos \alpha - l \cos \theta \cdot \dot{\theta}^2)}{ml(\sin^2 \theta + \kappa)} \quad (20) \\ \ddot{x} &= \frac{lm \sin \theta (1 + \kappa) \dot{\theta}^2 - \text{sgn}(\dot{x}) \mu f_n (1 + \kappa) + gm(\kappa \sin \alpha - \cos(\alpha + \theta) \sin \theta)}{m(\sin^2 \theta + \kappa)} \\ f_n &= \frac{\kappa m (g \cos \alpha - l \cos \theta \cdot \dot{\theta}^2)}{\sin \theta (\text{sgn}(\dot{x}) \mu \cos \theta + \sin \theta) + \kappa}. \end{aligned}$$

Importantly, when  $\mu < \mu_c$ , a new periodic solution begins to evolve, which involves transition to contact slippage, while the impact can still result in contact sticking at the post-impact time. Fig. 2 shows such a periodic solution in  $(\theta, \dot{\theta})$  plane, which was computed numerically for  $\mu=0.4 < \mu_c$ . The dashed curve indicates solution under contact slippage  $\dot{x} \neq 0$ , while the solid curve denotes solution under contact sticking. In order to assess the stability of this stick-slip periodic solution, the linearization eigenvalue of the Poincaré map was computed numerically under different coefficients of friction. Fig. 4 shows the eigenvalue  $\lambda$  as a function of the friction coefficient  $\mu$ . For  $\mu > \mu_c$ , the no-slip periodic solution is maintained, with eigenvalue of  $\beta^2=0.734$ . When  $\mu$  is decreased below  $\mu_c$ , both the initial condition of the periodic solution  $\dot{\theta}^*$  and the linearization eigenvalue  $\lambda$  change continuously. Remarkably, the stick-slip periodic solutions exist for a wide range of the friction coefficient  $\mu$ . Nevertheless, they are slightly less stable than the no-slip solution, with an increase of up to 5% in  $\lambda$ . At  $\mu=0.25$  the periodic solution disappears, because the impact can no longer maintain post-impact contact sticking  $\dot{x}_\#^+ = 0$  without exceeding the friction limitation (10).

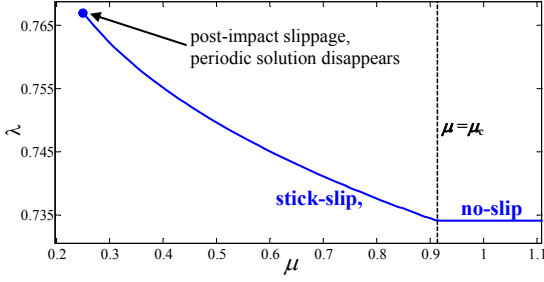


Fig. 4: Stability eigenvalue  $\lambda$  of the periodic solution vs.  $\mu$

#### IV. THE PASSIVE COMPASS BIPED

In this section, we analyze the dynamics of the passive compass biped under contact sticking and/or slippage of the foot. The compass biped is a robotic model which consists of two rigid links (“legs”) of length  $l$ , connected by a passive rotary joint (“hip”), see Fig. 5. For simplicity, we assume that the two legs have identical point masses  $m$  located at a distance  $d$  from their endpoints (“feet”). Another point mass  $m_h$  is located at the hip joint. The robot walks on an inclined plane with slope angle  $\alpha$ . The angle of the stance foot is  $\theta_1$  and the angle of the swing foot is  $\theta_2$ , both measured with respect to the contact normal ( $y$  axis). The robot’s coordinates are chosen as  $\mathbf{q}=(\theta_1, \theta_2, x, y)$ , where  $(x, y)$  denote the position of the stance foot. The equations of motion of the robot are given by (2), where

$$\mathbf{M} = \begin{bmatrix} d^2 m + l^2 (m + m_h) & lm(1-d)\cos(\theta_1 + \theta_2) & [dm + l(m + m_h)]\cos\theta_1 & -[dm + l(m + m_h)]\sin\theta_1 \\ lm(1-d)\cos(\theta_1 + \theta_2) & m(d-l)^2 & m(1-d)\cos\theta_2 & m(1-d)\sin\theta_2 \\ [dm + l(m + m_h)]\cos\theta_1 & m(1-d)\cos\theta_2 & 2m + m_h & 0 \\ -[dm + l(m + m_h)]\sin\theta_1 & m(1-d)\sin\theta_2 & 0 & 2m + m_h \end{bmatrix}$$

$$\mathbf{B} = \begin{bmatrix} (d-l)lm\sin(\theta_1 + \theta_2)\dot{\theta}_2^2 \\ (d-l)ml\sin(\theta_1 + \theta_2)\dot{\theta}_1^2 \\ (d-l)m\sin\theta_2\dot{\theta}_2^2 - ((d+l)m + lm_h)\sin\theta_1\dot{\theta}_1^2 \\ -lm_h\cos\theta_1\dot{\theta}_1^2 - (d+l)m\cos\theta_1\dot{\theta}_1^2 + (l-d)m\cos\theta_2\dot{\theta}_2^2 \end{bmatrix} \quad \mathbf{W} = \begin{bmatrix} 0 & 0 & 1 & 0 \\ 0 & 0 & 0 & 1 \end{bmatrix} \quad \mathbf{E}\mathbf{u} = 0$$

$$\mathbf{G} = g \begin{bmatrix} -((d+l)m + lm_h)(\sin\alpha\cos\theta_1 + \cos\alpha\sin\theta_1) \\ (d-l)m\sin(\alpha - \theta_2) \\ -(2m + m_h)\sin\alpha \\ (m_h + 2m)\cos\alpha \end{bmatrix} \quad \tilde{\mathbf{W}} = \begin{bmatrix} l\cos\theta_1 & l\cos\theta_2 & 1 & 0 \\ -l\sin\theta_1 & l\sin\theta_2 & 0 & 1 \end{bmatrix} \quad (21)$$

The swing foot hits the ground when  $\theta_1 = \theta_2$ , so that the three-dimensional Poincaré section  $\Sigma$  is characterized by the state variables  $(\theta_1, \dot{\theta}_1, \dot{\theta}_2)$ . Stable periodic solutions for the

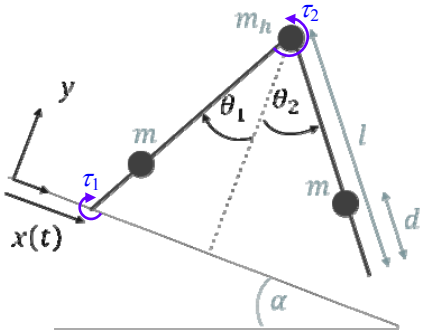


Fig. 5: The compass biped model (Passive:  $\tau_1 = \tau_2 = 0$ . Actuated:  $\tau_1, \tau_2 \neq 0$  and  $\alpha = 0$ )

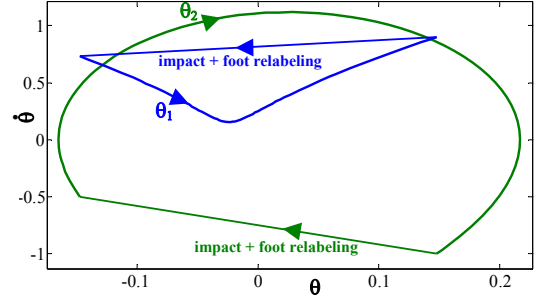


Fig. 6: Trajectories in  $(\theta, \dot{\theta})$  plane for the passive compass biped

compass biped have been demonstrated in [12] and extensively studied in [13], assuming sticking contact. As an example, we choose the parameter values  $l=0.8$ ,  $d=0.5$ ,  $m=4$ ,  $m_h=2$ ,  $g=9.8$ , and  $\alpha=1^\circ$ . Using numerical simulations, a periodic solution is found, which corresponds to the post-impact values  $\theta_1^* = -0.149$ ,  $\dot{\theta}_1^* = 0.733$  and  $\dot{\theta}_2^* = -0.501$ . The trajectories of  $\theta_1$  and  $\theta_2$  in  $(\theta, \dot{\theta})$  plane are shown in Fig. 6. The linearization matrix of the Poincaré map  $D\Pi(\mathbf{x}^*)$  has three eigenvalues, whose maximal absolute value is  $\lambda_{\max} = 0.71 < 1$ , indicating that the periodic solution is stable.

Next, we use (3) in order to compute the ratio  $\sigma$  of tangential-to-normal contact forces at the stance foot. The ratio  $\sigma(t)$  along the periodic solution is shown in Fig. 7 (solid curve). The plot indicates that the minimal value of friction coefficient required to enforce contact sticking is  $\mu_c = 0.175$ . Moreover, the ratio  $\tilde{\sigma}$  of the tangential-to-normal impulse at the impact is marked as 'X' at the right end of the plot, and its value is given by  $|\tilde{\sigma}| = 0.145 < \mu_c$ . This indicates that as long as  $\mu \geq \mu_c$ , the contact maintains sticking at the impact as well.

When the friction coefficient is decreased below the critical value  $\mu_c$ , a new periodic solution evolves, which involves transition to contact slippage. For small changes from  $\mu_c$ , the impact still satisfies  $|\tilde{\sigma}| \leq \mu$  and results in contact sticking. Therefore, the post-impact Poincaré section is still three-dimensional. Fig. 8 shows such a periodic solution (marked by A) for  $\mu=0.14 < \mu_c$ . The dashed curves indicate

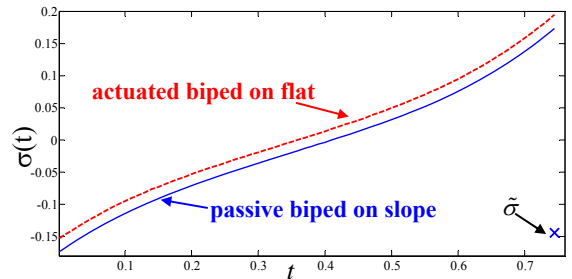


Fig. 7: The force ratio  $\sigma$  vs  $t$  along the periodic solution (solid – passive biped on a slope. dashed – actuated biped on flat)

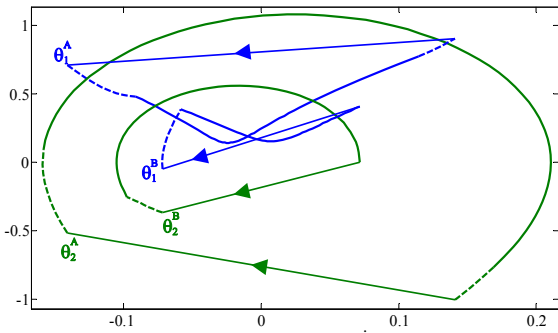


Fig. 8: Two types of trajectories in  $(\theta, \dot{\theta})$  plane for  $\mu=0.14$ : A. post-impact sticking, B. post-impact slippage

solutions under contact slippage  $\dot{x} \neq 0$ , while the solid curves denote solutions under contact sticking. In this periodic solution, the contact at the post-impact time is sticking, i.e.  $\dot{x}_{\#}^+ = 0$ . (The value of the impulse ratio  $\tilde{\sigma}$  changes with the periodic solution, and still satisfies  $|\tilde{\sigma}| \leq \mu$ ). The solution begins with an immediate transition to slipping forward, followed by switching to contact sticking, and then a transition to slipping backwards until the next impact. The maximal eigenvalue of  $D\Pi(\mathbf{x}^*)$  for this periodic solution was obtained as  $\lambda_{\max} = 0.8$ , indicating that the solution is still stable. Next, the friction coefficient was decreased continuously from  $\mu_c$  and the maximal eigenvalue  $\lambda_{\max}$  for the periodic solution was computed. Fig. 9 plots  $\lambda_{\max}$  as a function of  $\mu$  (solid curve). One can see that  $\lambda_{\max}$  increases upon decreasing  $\mu$ . At  $\mu=0.11$ ,  $\lambda_{\max}$  crosses 1 and the periodic solution becomes unstable.

In addition to this branch of periodic solutions with post-impact sticking  $\dot{x}_{\#}^+ = 0$ , numerical search reveals the co-existence of another type of periodic solutions with slippage at the post-impact time  $\dot{x}_{\#}^+ \neq 0$ . The initial slippage is followed by transition back to contact sticking, and then reaching impact. These periodic solutions have a four-dimensional post-impact Poincaré section  $\Sigma$ , which is characterized by the state variables  $(\theta, \dot{\theta}_1, \dot{\theta}_2, \dot{x})$ . A periodic solution of this type is shown for  $\mu=0.14$  in Fig. 8 (marked as B). The maximal linearization eigenvalue is  $\lambda_{\max}=2.76$ , indicating that this periodic solution is highly unstable. Periodic solutions of this type were also found in the range  $0.1 \leq \mu \leq 0.3$ , and their maximal eigenvalue  $\lambda_{\max}$  as a function of  $\mu$  is shown as the dashed curve in Fig. 9. It can be seen that these solutions are always unstable. Remarkably, these periodic solutions exist also for  $\mu > \mu_c$ . That is, they co-exist even with no-slip solutions for large friction.

## V. THE ACTUATED COMPASS BIPED

In this section, we analyze the dynamics of the compass biped walking on a horizontal plane and powered by actuation torques at the ankle joint (i.e. the stance foot's contact point) and the hip joint. We study both open-loop and closed loop control of the joint torques, and compare between the no-slip

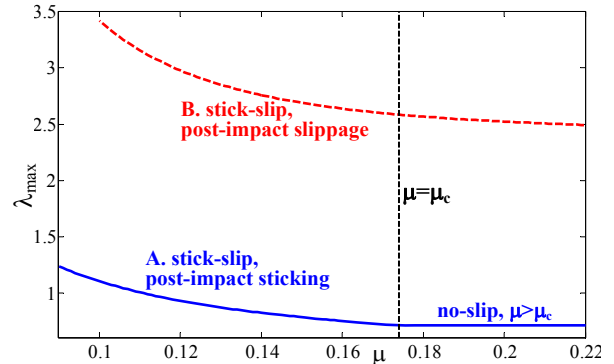


Fig. 9: Maximal eigenvalue  $\lambda_{\max}$  of the periodic solutions vs.  $\mu$

gait and the stick-slip gaits with and without post-impact slippage. In particular, we compute the energetic cost of walking, which was studied in [33]. The expressions in the equations of motion (2) of the actuated compass biped are almost identical to those in (21), with  $\alpha=0$  implying a horizontal plane, and the terms of the control torques given by

$$\mathbf{E} = \begin{bmatrix} 1 & 0 & 0 & 0 \\ 1 & 1 & 0 & 0 \end{bmatrix}^T, \quad \mathbf{u} = \begin{bmatrix} \tau_1 \\ \tau_2 \end{bmatrix}$$

where  $\tau_1$  is the ankle torque and  $\tau_2$  is the hip torque (Fig. 5).

**Gait I:** We begin by studying open-loop control of the actuation torques under contact sticking. A simple way to choose the torques  $\tau_1(t)$  and  $\tau_2(t)$  is prescribing a periodic trajectory of the joint angles  $\theta_i(t)$  and compute the corresponding input torques  $\mathbf{u}(t)$  by substituting  $\mathbf{q}(t), \dot{\mathbf{q}}(t)$  and  $\ddot{\mathbf{q}}(t)$  into (2). Fig. 10 plots the torques  $\tau_i(t)$  which are computed by choosing the trajectory of  $\theta_i(t)$  given in Fig. 6 on a horizontal plane, for the same values of physical parameters chosen in the previous section. Interestingly,  $\tau_i(t)$  display very small variations during the gait. Thus, we choose to approximate them by constant values as  $\tau_1=-2.73$  and  $\tau_2=0.54$ . (It is assumed that the robot is capable of detecting which foot is currently in contact, and applies the ankle torque  $\tau_1$  at that foot). This is also very convenient since the dynamic equations in (2) under constant input  $\mathbf{u}$  are time-invariant and one can find hybrid periodic solutions without restrictions on their time period. Using numerical search, a periodic solution in found (not shown), which is very close to the original

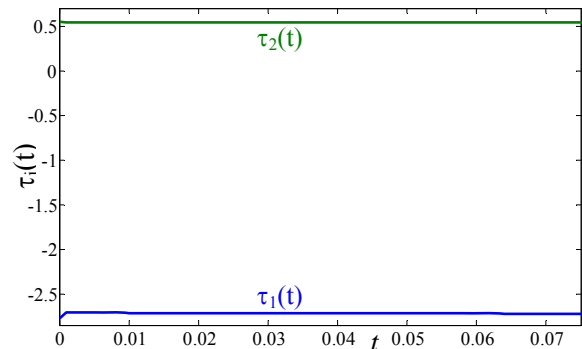


Fig. 10: Actuation torques  $\tau_i(t)$  along the no-slip periodic solution

solution appearing in Fig. 6. The maximal eigenvalue of the linearization matrix  $D\Pi(\mathbf{x}^*)$  is given by  $\lambda_{\max} = 0.713 < 1$ . (Very close to the original value  $\lambda_{\max} = 0.71$  which was obtained for the trajectory of the passive walker in Fig. 6.

The *specific cost* of a walking gait is defined in [33,34] as

$$c_{mt} = \frac{W}{mgS} = \frac{1}{mgS} \int_0^T \mathbf{E}\mathbf{u}(t) \cdot \dot{\mathbf{q}}(t) dt \quad (22)$$

where  $T$  is the period time,  $W$  is the total mechanical work expended by the actuators during a full period,  $S$  is the distance traveled in one period, and  $mg$  is the robot's weight. This quantity is not quite meaningful for *passive* walking on a slope (cf. [34]), but can be used to compare different gaits of actuated walking. For the open-loop gait with constant actuation torques, the specific cost was computed as  $c_{mt}=0.0173$ . The *average speed* of this gait, defined as  $\bar{v} = S/T$ , was obtained as  $\bar{v} = 0.63$ .

Next, we compute the ratio of tangential-to-normal forces  $\sigma(t)$  along this open-loop gait, which is plotted as a dashed curve in Fig. 7. One can see that the critical value of friction coefficient required in order to prevent slippage is  $\mu_c=0.194$ . When the friction coefficient is decreased below  $\mu_c$  a periodic gait with stick-slip transition begins to evolve, with sticking at the post-impact time. As a result, the specific cost  $c_{mt}$  of the gait changes with  $\mu$ , as plotted in Fig. 11 (solid curve). One can see that upon decreasing  $\mu$ ,  $c_{mt}$  is first increasing, and then decreasing. The reason for this behavior can be understood from the shape of  $\sigma(t)$  in Fig. 7, which indicates that when  $\mu$  is slightly lower than  $\mu_c$ , backward slippage evolves at the end of the gait, and when  $\mu$  is further decreased, additional forward slippage evolves at the beginning of the gait which compensates for the backwards slippage and slightly improves the energetic efficiency. Interestingly, upon decreasing  $\mu$ , the average speed  $\bar{v}$  is monotonically decreasing (not shown), and the maximal stability eigenvalue  $\lambda_{\max}$  is increasing until the gait becomes unstable for  $\mu=0.103$ , as shown in Fig. 12 (solid curve).

**Gait II:** Similar to the passive biped, one can generate a gait with post-impact slippage for the actuated biped. This is done by taking the kinematics of  $\theta_i(t)$  along a gait similar to

the one from Fig. 8 (gait B), compute the required torques  $\tau_i(t)$  according to (2), and approximate them by constant values, which are given by  $\tau_1=-0.69$  and  $\tau_2=0.12$ . Applying these torques under friction coefficient of  $\mu=0.2$ , one obtains a periodic gait with post-impact slippage, as expected. Remarkably, this gait is very efficient, and has  $c_{mt}=0.0044$ , which is 4-fold smaller than the cost of the no-slip gait. On the other hand, the average speed of this gait is  $\bar{v} = 0.31$ , which is twice slower than the actuated no-slip gait. An explanation to the decrease in  $\bar{v}$  is that the angles  $\theta_1=\theta_2$  at the impact, which directly affect the step length, are reduced by half from the post-impact sticking gait A to post-impact slipping gait B (see Fig. 8), while the change in the period time is much smaller (0.75 to 0.7). More importantly, this gait is *unstable*, with maximal eigenvalue  $\lambda_{\max} = 1.225$ , thus it cannot be practically implemented.

**Gait III:** In order to exploit the improved energetic efficiency of the post-impact slipping gait while avoiding the problem of its instability, the next step is to introduce a *closed-loop feedback law* for the actuation torques, as follows. As before, we choose a periodic reference trajectory of the joint angles  $\theta_1^r(t)$ ,  $\theta_2^r(t)$ , which are taken from gait B in Fig. 8 with post-impact slippage. The actuation torques are then determined by a PD control law with *phase resetting* [35,36] as:  $\tau_i = -k_p (\theta_i(\phi) - \theta_i^r(\phi)) - k_d (\dot{\theta}_i(\phi) - \dot{\theta}_i^r(\phi))$ , where

$\phi = t - t_{\#}$  is the *phase* of the gait with respect to the time of the last impact  $t_{\#}$ . It is assumed here that the robot can detect the impact event and immediately “reset” the time of the reference trajectory. Note that even though this control law results in a non-autonomous dynamical system, it still enables obtaining periodic solutions without restrictions on their time period. Applying this control law with  $k_p=k_d=15$  under  $\mu=0.2$  results in a periodic gait with post-impact slippage which is different from the reference trajectory. This gait has specific cost of  $c_{mt}=0.0055$ , which is slightly less efficient than the open-loop actuated gait. Nevertheless, the maximal stability eigenvalue is  $\lambda_{\max} = 0.37$ , so that the gait is highly stable. The specific cost  $c_{mt}$  for the three different controls as a function of  $\mu$  is shown in Fig. 11, while the maximal stability eigenvalue  $\lambda_{\max}$  is shown in Fig. 12. One can see that the feedback control law stabilizes the energetically efficient gait of post-impact slippage. Importantly, the gait exists under the same control

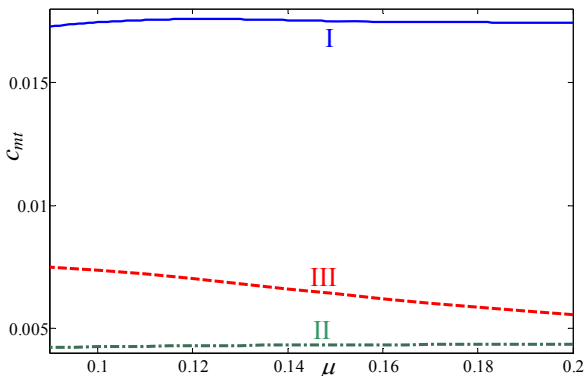


**Fig. 11:** The specific cost of transport  $c_{mt}$  vs.  $\mu$  for three controls: **I.** open-loop, post impact sticking. **II.** open-loop, post-impact slippage **III.** PD control, post impact slippage

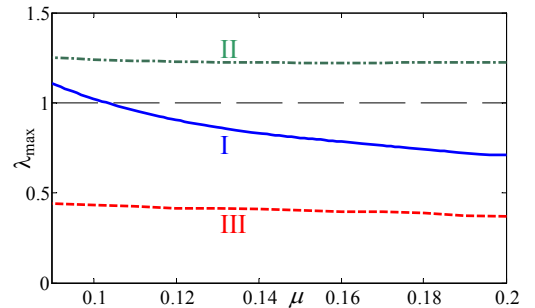


**Fig. 12:** Maximal stability eigenvalue  $\lambda_{\max}$  vs.  $\mu$  for three controls: **I.** open-loop, post impact sticking. **II.** open-loop, post-impact slippage **III.** PD control, post impact slippage

law and reference trajectory for a wide range of the friction coefficient  $\mu$ , including also  $\mu > \mu_c$ . That is, this control law is robust with respect to changes in  $\mu$ , and indirectly enforces foot slippage even for large friction for which a non-slipping gait co-exists. One challenging open problem is a systematic design of the reference trajectory in order to enlarge the step length and improve both speed and efficiency.

## VI. CONCLUSION

In this paper, we numerically investigated simple and low-dimensional models of dynamic bipedal walking under possible foot slippage. We have found stable and unstable periodic solutions with stick-slip transitions for passive walking of the rimless wheel and the compass biped models. For the actuated compass biped on a horizontal plane, we have shown that a PD control law with phase reset can stabilize a co-existing (otherwise unstable) periodic gait with post-impact slippage, yielding decrease in the average speed and significant improvement in the energetic efficiency. The performance of this control law is remarkably robust with respect to changes in the friction coefficient, and enforces foot slippage even for large friction. To conclude, the influence of foot slippage on dynamic legged locomotion is far from being completely understood, but the present work showed an initial glimpse into this challenging problem, and will hopefully motivate further investigation.

## REFERENCES

- [1] M. Raibert, K. Blankespoor, G. Nelson, R. Playter and the BigDog Team, "BigDog, the rough-terrain quadruped robot". Proceeding of the 17th IFAC World Congress, pp.10822-10825, 2008.
- [2] J. R. Reubla, P. D. Neuhau, B. V. Bonnländer, M. J. Johnson, and J. E. Pratt, "A controller for the LittleDog quadruped walking on rough terrain". In IEEE Int. Conf. on Robotics and Automation, pages 1467-1473, 2007.
- [3] K. Hirai, M. Hirose, Y. Haikawa, and T. Takenaka, "The development of Honda humanoid robot". In IEEE Int. Conf. on Robotics and Automation, pages 1321-1326, 1998.
- [4] G. Aguirre-Ollinger, J. E. Colgate, M. A. Peshkin and A. Goswami, "Inertia compensation control of a one-degree-of-freedom exoskeleton for lower-limb assistance: Initial experiments", IEEE Trans. Neural Systems and Rehabilitation Engineering, vol. 20, no. 1, pp. 68-77, 2012.
- [5] E. Krotkov and R. Simmons, "Perception, planning, and control for autonomous walking with the Ambler planetary rover". Int. Journal of Robotics Research, 16:155-180, 1996.
- [6] B. H. Wilcox *et al* "ATHLETE: A cargo handling and manipulation robot for the moon". J. of Field Robotics, 24(5):421-434, 2007.
- [7] M. Dickinson, C. Farley, R. Full, M. Koehl, R. Kram, and S. Lehman, "How animals move: An integrative view", Science 288:100-106, 2000.
- [8] P. Holmes, R. Full, D. Koditschek, and J. Guckenheimer, "The dynamics of legged locomotion: Models, analysis and challenges", SIAM Review, 48(2):207-304, 2006.
- [9] U. Saranlı, M. Buehler, and D. E. Koditschek, "RHex: A simple and highly mobile hexapod robot", International Journal of Robotics Research, 20(7):616-631, 2001.
- [10] R. Goebel, R. G. Sanfelice, and A. R. Teel, "Hybrid dynamical systems," IEEE Control Systems Magazine, 29(2):28-93, 2009.
- [11] B. Brogliato, *Nonsmooth Mechanics*, Springer-Verlag, 1999.
- [12] T. McGeer, "Passive dynamic walking". The International Journal of Robotics Research, 9(2):62-82, 1990.
- [13] A. T. Goswami, "A study of the passive gait of a compass-like biped robot: Symmetry and chaos", The International Journal of Robotics Research, pp. 1282-1301, 1998.
- [14] M. J. Coleman and A. Ruina, "Dynamics and stability of a rimless spoked wheel: a simple 2D system with impacts", Dynamical Systems: an International Journal, Volume 25, Number 2, pp. 215-238, 2010.
- [15] J. Guckenheimer and P. Holmes, *Nonlinear oscillations, dynamical systems, and bifurcations of vector fields*, Springer-Verlag, NY, 1983.
- [16] Y. Hurmuzlu, F. Génot and B. Brogliato, "Modeling, stability and control of biped robots - a general framework", Automatica, 40(10):1647-1664, 2004.
- [17] E. R. Westervelt, J. W. Grizzle, C. Chevallereau, J. H. Choi, and B. Morris, *Feedback Control of Dynamic Bipedal Robot Locomotion*, CRC Press, 2007.
- [18] M. W. Spong and F. Bullo, "Controlled symmetries and passive walking", IEEE Trans. on Automatic Control, 50(7):1025-1031, 2005.
- [19] R. D. Gregg and M. W. Spong, "Reduction-based control of three-dimensional bipedal walking robots", The International Journal of Robotics Research, 29(6):680-702, 2010.
- [20] E. Westervelt, J.W. Grizzle, and D.E. Koditschek, "Hybrid zero dynamics of planar biped walkers", IEEE Transactions on Automatic Control, 48(1):42-56, 2003.
- [21] L. B. Freidovich, A. S. Shiriaev and I. R. Manchester, "Stability analysis and control design for an underactuated walking robot via computation of a transverse linearization", Proceeding of the 17th IFAC World Congress, pp.10166-10171, 2008.
- [22] C. Canudas-de-Wit, "On the concept of virtual constraints as a tool for walking robot control and balancing", Annual Reviews in Control, Volume 28, Issue 2, Pages 157-166, 2004.
- [23] H. L. McClintchey, J. J. Thomason and R.J. Runciman, "Grip and slippage of the horse's hoof on solid substrates measured ex vivo", Biosystems Engineering 89(4):485-494, 2004.
- [24] A. J. Clark and T. E. Higham, "Slipping, sliding and stability: locomotor strategies for overcoming low-friction surfaces", J. Experimental Biology 214:1369-1378, 2011.
- [25] T. H. Chang and Y. Hurmuzlu, "Sliding control without reaching phase and its application to bipedal locomotion. ASME J. Dynamic Systems, Measurement, and Control, 105:447-455, 1994.
- [26] S. Kajita *et al*, "Biped walking on a low friction floor", Proc. IEEE/RSJ Int. Conf. Intelligent Robots and Systems, (IROS), pp. 3546-3552, 2004.
- [27] K. Kaneko *et al*, "Slip observer for walking on a low friction floor", Proc. IEEE/RSJ International Conference on Intelligent Robots and Systems, (IROS), pp. 634-640, 2005.
- [28] M. D. Berkemeier and R. S. Fearing, "sliding and hopping gaits for the underactuated acrobot", IEEE Trans. Robotics and Automation, 14(4):629-634, 1998.
- [29] R. M. Murray, Z. Li, and S. Sastry, *A Mathematical Introduction to Robotic Manipulation*, CRC press, Boca Raton, FL 1994.
- [30] F. Pfeiffer and C. Glocker, *Multibody Dynamics with Unilateral Contacts*, Wiley & Sons, 1996.
- [31] A. Chatterjee and A. Ruina, "A new algebraic rigid body collision law based on impulse space considerations", ASME J. Appl. Mech., vol. 65, no. 4, pp. 939-951, 1998.
- [32] M. Garcia, A. Chatterjee, A. Ruina, and M. Coleman, "The simplest walking model: Stability, complexity and scaling", ASME J. Biomech. Eng., 120 (1998), pp. 281-288.
- [33] S. Collins, A. Ruina, R. Tedrake and M. Wisse, "Efficient bipedal robots based on passive dynamic walkers", Science 307:1082-1085, 2005.
- [34] M. Garcia, A. Chatterjee and A. Ruina, "Efficiency, speed, and scaling of two-dimensional passive-dynamic walking", Dynamics and Stability of Systems, Vol. 15, No. 2, Pages 75-99, 2000.
- [35] S. Aoi and K. Tsuchiya, "Stability analysis of a simple walking model driven by an oscillator with a phase reset using sensory feedback", IEEE Transactions on Robotics, 22(2):391-397, 2006.
- [36] T. Nomura, K. Kawa, Y. Suzuki, M. Nakanishi and T. Yamasaki, "Dynamic stability and phase resetting during biped gait", Chaos 19:026103, 2009.